Journal of Hazardous Materials 415 (2021) 125749

Contents lists available at ScienceDirect

Journal of Hazardous Materials

journal homepage: www.elsevier.com/locate/jhazmat

Adsorption performance and mechanism of iron-loaded biochar to methyl orange in the presence of Cr^{6+} from dye wastewater

Han Cheng [a], Yali Liu [a,*], Xin Li [b]

[a] School of Civil Engineering, Nanjing Forestry University, Nanjing 210037, China
[b] School of Environment, Harbin Institute of Technology, Harbin 150090, China

ARTICLE INFO

Editor: Dr. H. Artuto

Keywords:
Sewage sludge
Hybrid liriodendron
Adsorption kinetics
Equilibrium isotherms
Competitive adsorption

ABSTRACT

Biochar prepared from sludge and liriodendron leaves (SLAC) was modified by Fe^{3+} (SLAC-Fe), and they were used to remove methyl orange (MO) from single system and aqueous solution with Cr^{6+}. The physical and chemical properties of biochar were characterized by BET, SEM, TEM, EDS, FTIR and XPS. The influences of initial MO concentration, adsorbent dose, pH, contact time and temperature on the adsorption of MO by biochar were investigated. The results indicated that SLAC-Fe had a higher removal efficiency for MO than SLAC. In the binary system, the maximum adsorption capacities of MO were 0.26 and 0.22 mmol/g with Cr^{6+} concentrations of 0.2 and 0.8 mmol/L, respectively. The adsorption kinetic model of pseudo-second-order fitted well with the experimental data of MO in single system. The equilibrium experimental data of MO in single and binary component systems were fitted well to Freundlich isotherm models. It was based on chemical and multilayer adsorption. It could be concluded that there was a competitive adsorption between Cr^{6+} and MO. The reason was that the $HCrO_4^-$ and $Cr_2O_7^{2-}$ competed with SO_3^- for the effective adsorption sites on the surface of SLAC-Fe, resulting in a reduction in the adsorption capacity of MO.

1. Introduction

Organic dyes are widely used in textile, printing, dyeing, electroplating, papermaking, food processing and other industries (Jawad et al., 2019). The discharge of dye wastewater has caused great pollution to the water environment. The anionic dye methyl orang (MO) is one of the most common pollutants. Due to the high biological oxygen demand (BOD), high toxicity and poor biodegradability of MO, it seriously affects the photosynthesis of aquatic plants and the growth of animals in the water and ecosystem (Kafshgari et al., 2017). Therefore, effective removal of MO is of great importance to environmental protection and human health. To date, a variety of technologies, such as chemical precipitation, ion-exchange, electrochemical process, photocatalytic reduction and adsorption, have been developed to reduce MO from aquatic environment (Tian and Yang, 2007; Gholami et al., 2020; Qiu et al., 2020; Setshedi et al., 2013). Among them, adsorption has been widely used because of its advantages of simple equipment, low price, high efficiency, and the ability to adsorb various pollutants (Ma et al., 2019).

However, dye wastewater is a multi-component system, in which other organic pollutants or heavy metals have important influences on the adsorption of MO (Ding et al., 2020). It has been proved that, in the binary-component system, there were synergistic promotion effects between congo red/Cd^{2+} with MO (Zhang et al., 2016; Zou et al., 2016). In addition, it is reported that Cr^{6+} was often used as mordant in printing and dyeing, which competed with other pollutants in the dye wastewater for the active sites of activated carbon (Ding et al., 2020; Yu et al., 2020). This competitive relationship in the adsorption processes resulted in a decrease in the removal rate of target adsorbate and an increase in the dosage of activated carbon (Luna et al., 2010; Qiu et al., 2018). Coupled with the fact that the commercial activated carbon was preparade from non-renewable energy such as wood, shells and coal (Zhang et al., 2020). The application of commercial activated carbon in actual sewage was restricted.

Therefore, great efforts have been made to prepare adsorbents from renewable and low-cost biomass (Ma et al., 2019; Devi and Saroha, 2017; Silva et al., 2018; Wang et al., 2020). Sludge is an inevitable by-product of wastewater treatment plant (WWTP). In China, the emissions in 2015 were about 53.52 billion tons (moisture content: 85%) (Chen et al., 2019). The sludge is cheap, easy to be obtained, and rich in organic matters (30–70%), so the preparation of biochar from sludge has been regarded to be a promising disposal method

* Corresponding author.
E-mail addresses: deji1116@163.com (H. Cheng), liuyali0418@163.com (Y. Liu), lixinharbin@163.com (X. Li).

https://doi.org/10.1016/j.jhazmat.2021.125749
Received 29 October 2020; Received in revised form 25 February 2021; Accepted 21 March 2021
Available online 26 March 2021
0304-3894/© 2021 Elsevier B.V. All rights reserved.

(Ruiz-Gomez et al., 2017). Nevertheless, a large amount of ash and inorganic substances were contained in the sludge, which led to the underdeveloped surface void structure and low adsorption efficiency of sludge-based biochar (Silva et al., 2018). In order to improve the surface area and internal pore structure of sludge-based biochar, various types of agricultural wastes rich in lignin, cellulose and hemicellulose were added into sludge, such as hazelnut shells (Ferrero, 2007), sugar beet bagasse (Ghorbani et al., 2020), apple peels (Enniya et al., 2018), rice husk (Alam et al., 2020), and leaves.

On the other hand, some methods were used to derive new functional groups on the surface of activated carbon to improve its chemical properties (Ma et al., 2019; Devi and Saroha, 2017; Silva et al., 2018; Zhong et al., 2020). In recent years, the removal of metal ions and organic substances by loading metal onto biochar has attracted widespread attention (Sugashini and Begum, 2014). Nanometer zinc (Gan et al., 2015), MnOx (Lian et al., 2014), aluminum (Qian et al., 2013), ferric iron (Agrafioti et al., 2014; Zhong et al., 2020), were used for the modification of biochar, in which iron was often chosen due to its low price and secondary hydrolysis effect (Liu et al., 2010; Fierro et al., 2009). As previously reported in the literature, the magnetic biochar loaded with Fe_3O_4 improved the removal rate and adsorption capacity of Cr^{6+} by providing electrons to reduce Cr^{6+} to Cr^{3+}(Zhong et al., 2018; Zhou et al., 2018). Simultaneously, reduced Cr^{3+} combined with the -OH on the surface of biochar to precipitate $Cr(OH)_3$ (Valentin-Reyes et al., 2019). At the same time, the iron-loaded adsorbent have achieved good results in the polydye wastewater (Hu et al., 2017).

Consequently, in this study, both liriodendron leaves and Fe^{3+} were used to modify the physical and chemical properties of biochar produced from sludge (SLAC-Fe). Simultaneously, adsorption experiments of SLAC-Fe and biochar prepared from liriodendron leaves and sludge (SLAC) for MO removal from an aqueous solution containing Cr^{6+} were conducted. The optimal operational parameters such as biochar dose, pH, initial concentration, contact time and temperature for effective adsorption of MO were investigated. Meanwhile, kinetic models (the pseudo-first-order, the pseudo-second-order), and isotherm models (Langmuir, Freundlich and Temkin models) were used to evaluate the adsorption process. The specific surface area and pore diameter distribution of biochar were measured by Brunauer-Emmett-Teller (BET). In addition, the adsorption mechanism of MO was determined by analyzing the physical and chemical properties of biochar using scanning electron microscopy (SEM), transmission electron microscopy (TEM), energy dispersive spectrometry (EDS), Fourier Transform Infrared Spectrometer (FTIR) and X-ray photoelectron spectroscopy (XPS).

2. Materials and methods

2.1. Biochar preparation

The sludge and liriodendron leaves were used to prepare biochar. The sludge was obtained from a dewatering room of Qiaobei WWTP in Nanjing, China. The liriodendron leaves were collected from Nanjing Forestry University, China.

The detailed preparation process of biochar was as follows: At first, the sludge and liriodendron leaves were dried to a constant weight at 110 °C using a drying oven (DGG-9030A, Dong Lu, Shanghai, China), and then crushed and sieved to below 50-mesh. The dried sludge and liriodendron leaves were mixed in a 250 mL beaker and then impregnated in a 3 mol/L of $ZnCl_2$ solution (raw material: $ZnCl_2$ = 1: 3, m/m) at 25 °C for 24 h. Then the mixture was centrifuged at 3000 r/min for 6 min and the sediment was dried at 110 °C for 8 h. The dried mixture was carbonized in muffle furnace at 550 °C for 45 min (heating rate 5 °C/min) (SX-12-10, Shi Yan, Shanghai, China). This activated material was washed with 1 mol/L of HCl solution, and then washed several times with ultra-pure water until the pH of the ultra-pure water was 7. Then, it was dried at 110 °C for 8 h and pulverized to below 50-mesh to obtain SLAC sample.

The SLAC was soaked in 0.002 mol/L $FeCl_3$ solution (SLAC: $FeCl_3$ = 1: 4, m/m) for 24 h, and the temperature was maintained at 110 °C. The product was washed with ultra-pure water till a pH of 7. Then, it was dried at 110 °C for 8 h and crushed to below 50-mesh to obtain SLAC-Fe.

2.2. Chemicals

Sodium hydroxide, MO, 36% hydrochloric acid, 95% sulfuric acid, acetone and 99.8% potassium dichromate were bought from Nanjing Chemical Reagent Co., Ltd., Nanjing, China. The molecular weights of Potassium dichromate and MO are 294.18 g/mol and 327.33 g/mol, respectively. The ultra-pure water was gained from the ultra-pure water machine (Biosafer-20TAB, Sai Fei, China).

2.3. Batch tests

2.3.1. Stock solution preparation

In a single system, a stock solution containing MO with a concentration of 1000 mg/L was prepared. In the binary system, the concentrations of Cr^{6+} and MO in the stock solution were both 20 mmol/L. That is, 2.8287 g of potassium dichromate and 6.5466 g of MO were weighed with an analytical balance (FA2004B, Yue ping, Shanghai, China), and then dissolved in 1000 mL of ultra-pure water.

2.3.2. Adsorption experiments

Batch adsorption experiments were carried out in a series of 250 mL conical flasks. Each flask was filled with 100 mL MO solution and a certain amount of biochar. The mixture was shaken using a thermostatic shaker incubator (300 r/min). The effects of different adsorption parameters, such as initial pH (2–10), contact time (0–240 min), biochar dosage (1–6 g/L), initial concentration (40–120 mg/L) and temperature (15–55 °C) on adsorption process were investigated. The pH value was adjusted by 0.5 (mol/L) of hydrochloric acid (aqueous solution) and 0.5 (mol/L) of sodium hydroxide (aqueous solution).

For the binary-component system, the initial concentration of MO varied in the range of 0.1–0.8 mmol/L, while the concentrations of Cr^{6+} were controlled at 0.2 and 0.8 mmol/L respectively. Simultaneously, 4 g/L of SLAC-Fe was added into each solution, the initial pH value was adjusted to 4.0, and the experiments were stirred for 30 min at 25 °C.

The samples taken from flasks at regular intervals were filtered through 0.45 μm Millipore HA membranes, and the concentrations of Cr^{6+} and MO in the filtrate were analyzed by UV-Vis spectrophotometer (L5S, Shanghai, China) at 540 nm and 460 nm wavelength, respectively.

The remove efficiency (E, %) of Cr^{6+} or MO was calculated using Eq. (1), and the equilibrium adsorption capacity q_e (mg/g) was given by the Eq. (2):

$$E = \frac{C_i - C_e}{C_i} \times 100\% \tag{1}$$

$$q_e = \frac{(C_i - C_e)}{W} \times V \tag{2}$$

Where q_e (mg/g) represented the adsorbed amount of Cr^{6+} or MO at equilibrium, C_e and C_i denoted equilibrium and initial concentration of Cr^{6+} or MO (mg/L), respectively, V was the volume of Cr^{6+} or MO solution (L), and W was the weight of biochar (g).

In this study, all the experiments were conducted in triplicate with average and standard deviation reported.

2.4. Analysis methods

The surface morphology, size and structure of the biochar were examined by field emission SEM (JSM-7600F, Japan) and transmission electron microscope TEM (JEM-1400, Japan). The porosity and surface area of biochar were measured by the surface area pore analyzer (V-Sorb 2800, GAPP, Beijing, China). The BET surface area (S_{BET}) was calculated

by equation of BET. The surface functional groups on the biochar were analyzed using FTIR (VERTEX 80 V, Brooke, German), and the spectra were obtained from 4000 to 400 cm^{-1}. The chemical state of the biochar surface was identified by XPS (AXIS Ultra DLD, Dao Jing, UK). The pH was measured by a pH meter (PHS-3C, Lei Ci, Shanghai, China).

2.5. Models for equilibrium

2.5.1. Langmuir isotherm

The Langmuir isotherm is expressed as follows:

$$q_e = \frac{Q_0 K_L C_e}{1 + K_L C_e} \tag{3}$$

Where Q_0 (mmol/g) is the maximum adsorbed amount of pollutant per unite weight of adsorbent, and the K_L (L/mmol) is the Langmuir constant.

K_L is related to the affinity of the binding sites. In a binary-systems, a higher value of K_L indicates that the solute is easier to be adsorbed. Langmuir isotherm illustrates the monolayer adsorption on the surface of adsorbent (Aksu et al., 2002).

2.5.2. Freundlich isotherm

The Freundlich isotherm is an empirical equation and different from the Langmuir isotherm, which is applied to multilayer adsorption.

The Freundlich isotherm is shown in Eq. (4):

$$q_e = K_F C_e^{1/n} \tag{4}$$

K_F and n are the Freundlich constants.

2.5.3. Temkin isotherm

The Temkin isotherm model assumes that the decrease of adsorption heat is a function of the temperature and the linear equation of the Temkin isotherm is given by Eq. (5):

$$q_e = \frac{RT}{\alpha_T}\ln(K_T) + \frac{RT}{\alpha_T}\ln(C_e) = B\ln(K_T) + B\ln(C_e) \tag{5}$$

Where R is the universal gas constant, 8.314 (J/(mol/K)); α_T (J/mol) is the Temkin isotherm constant; K_T (L/mg) is the Equilibrium binding constant related to the maximum binding energy.

2.6. Models for kinetic studies

The adsorption kinetics were analyzed by pseudo-first-order and pseudo-second-order kinetic models. The linear forms of pseudo-first-order and pseudo-second-order kinetic models are shown in Eq. (6) and Eq. (7), respectively.

$$\ln(q_e - q_t) = \ln q_e - k_1 t \tag{6}$$

$$\frac{t}{q_t} = \frac{1}{k_2 q_e^2} + \frac{t}{q_e} \tag{7}$$

Where, q_t is the adsorption amounts (mg/g) of the adsorbate at time t (min). The k_1 (1/min) and k_2 (g/(mg/min)) are the rate constants, respectively.

3. Results and discussion

3.1. Characterization of SLAC and SLAC-Fe

3.1.1. BET surface area

The specific surface area, pore structure distribution and porosity of SLAC and SLAC-Fe were studied by N_2 adsorption-desorption isotherms. The isotherm of the biochar samples and the corresponding aperture distribution curve are shown in Fig. 1. According to the International Union of Pure and Applied Chemistry (IUPAC) classification, the shapes

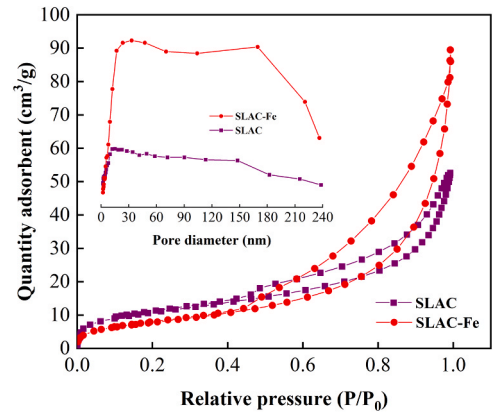

Fig. 1. N_2 adsorption-desorption isotherm of SLAC and SLAC-Fe.

of isotherms and hysteresis loops of SLAC and SLAC-Fe were classified as Type II with H3 hysteresis. This indicated that there was mesoporous structure in the SLAC and SLAC-Fe. In addition, when the relative pressure (P/P_0) was > 0.80, the adsorption capacities of these two biochar samples increased rapidly, which might be responsible for multilayer adsorption (Zhao et al., 2015).

The pore size distribution curves (the inset in Fig. 1.) showed that the pore diameter varied in the range of 0–240 nm. The pore structure of SLAC and SLAC-Fe are listed in Table 1. The S_{BET} and average pore diameter (D_p) values of SLAC were 39.485 m^2/g and 7.800 nm, respectively, and the corresponding values of SLAC-Fe were 45.206 m^2/g and 12.565 nm. The total pore volume (V_T) value of SLAC-Fe was (0.142 cm^3/g), which was much higher than that of SLAC (0.077 cm^3/g). These results indicated that the pores in SLAC and SLAC-Fe mainly existed in the form of mesopores. Compared with SLAC, the increase in the specific surface area of SLAC-Fe was mainly due to the fact that iron-loaded promoted the formation of pores.

3.1.2. SEM and TEM analyses

The surface morphology of biochar was studied by SEM. As displayed in Fig. 2(a), there were many small impurity particles on the surface of SLAC. Also, it is obvious that the surface of SLAC was loose and the pores were underdeveloped. On the contrary, the surface of SLAC-Fe was relatively smooth and had a large number of pores (in Fig. 2(b)). It can be inferred that SLAC-Fe had a better porous structure than SLAC, which was benefit for providing more adsorption sites for adsorbates. In addition, the distribution of iron element on the surface of SLAC-Fe is shown in Fig. 2(c). After the modification of Fe^{3+}, no obvious agglomeration phenomenon was observed on the SLAC-Fe. Simultaneously, the Fe content (28.03%) in SLAC-Fe demonstrated that Fe was successfully loaded on the biochar. The element analysis also suggested the proportion of C, N and Si in the SLAC-Fe were 43.07%, 10.21% and 18.69%, respectively, which was related to the addition of leaves.

TEM was used to further investigate the changes of the internal morphology of SLAC and SLAC-Fe. As can be seen in the Fig. 3(a), the addition of leaves made the biochar have a regular shape and flake accumulation, which promoted the development of pores. After loading iron salt, the pore structure of SLAC-Fe was obviously formed, and the pore size decreased (Fig. 3(b)). This might be caused by the loaded Fe^{3+} in the pores (Tuna et al., 2013). Meantime, the needle-like crystal structure was observed on the surface of SLAC-Fe. Combined with

Table 1
Characteristics of porous structure of SLAC and SLAC-Fe.

Samples	S_{BET} (m^2/g)	V_T (cm^3/g)	D_p (nm)
SLAC	39.485	0.077	7.800
SLAC-Fe	45.206	0.142	12.565

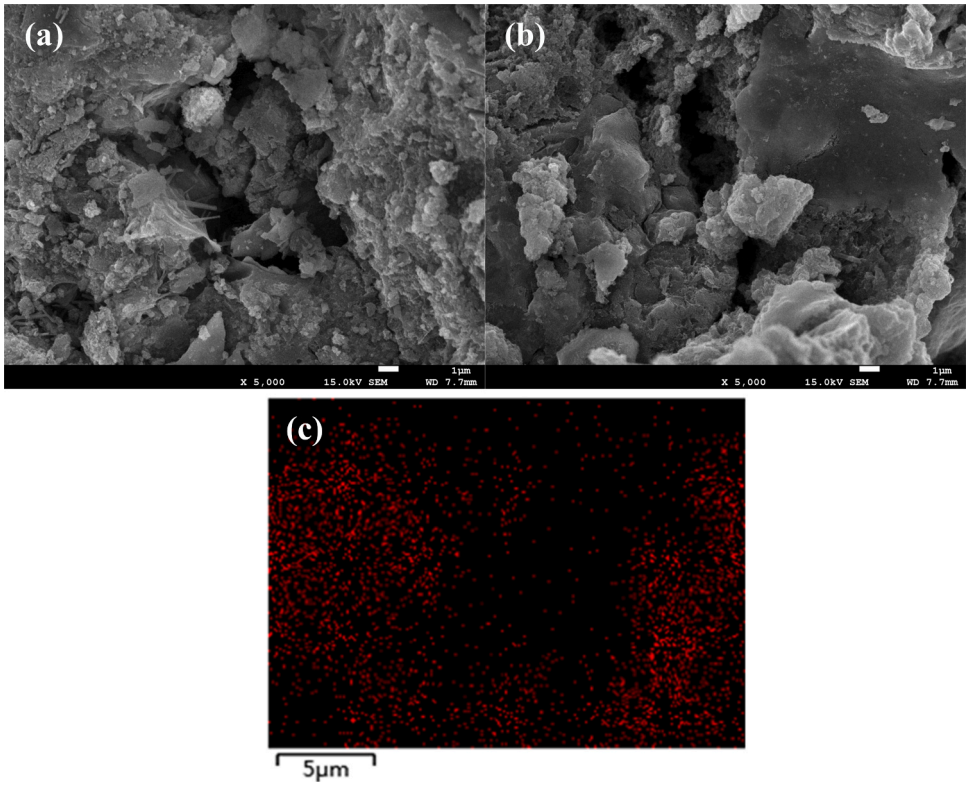

Fig. 2. SEM images of (a) SLAC, (b) SLAC-Fe and (c) the distribution of iron.

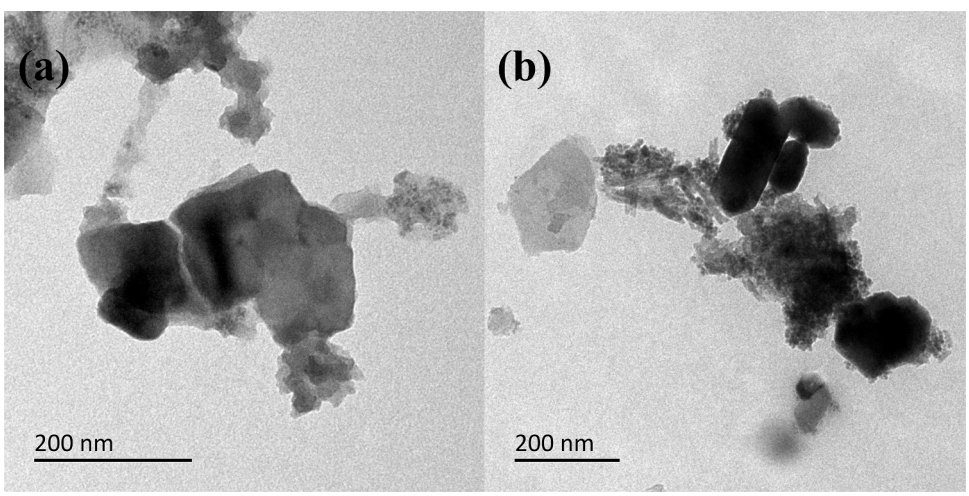

Fig. 3. TEM images of (a) SLAC and (b) SLAC-Fe.

following FTIR spectrum analysis, the main components of goethite were Fe_2O_3 and Fe_3O_4. It can be seen that the pore structure and chemical composition of biochar could be improved by adding leaves and loading iron ions.

3.1.3. FTIR analysis

The functional groups on the SLAC-Fe before and after adsorption were predicted by FTIR. FTIR analyses of SLAC-Fe (Fig. 4) showed a strong -OH (hydroxyl groups) stretching vibration group band at 3436 cm^{-1}, and the peak at 1634 cm^{-1} with moderate intensity described the stretching vibration N–H (Ding et al., 2020; Nur et al., 2014). The peak around 1400 cm^{-1} in the SLAC-Fe spectrum was caused by $-NH_2$ bending vibration of the amino group (Mahmoud et al., 2020). The Si–O–Si was characterized by the weak intensity peak at 1097 cm^{-1}. The Fe–O stretch vibration of Fe_2O_3 and Fe_4O_3 appeared at 593 cm^{-1}, indicating that the iron ions have been incorporated into biochar (Thuy Chung et al., 2015). In the FTIR spectrum of the SLAC-Fe/MO, the adsorption peaks described in SLAC-Fe were also observed, but the intensities were changed and shifted. Moreover, the new bands located at 2975, 2896, and 1048 cm^{-1} were ascribed to the stretching vibration of C–H, anti-symmetric, and $-SO_3^-$ symmetrical, respectively. The distinctive peak at 880 cm^{-1} could be attributed to the stretching and bending vibration of C–O. The above changes showed that functional groups played a role in the adsorption process of MO. Especially, the appearance of new functional groups indicated that MO has been successfully adsorbed.

In addition, after SLAC-Fe adsorbed the MO and Cr^{6+} from the binary system, the main functional groups, such as -OH, N–H, and $-NH_2$ shifted,

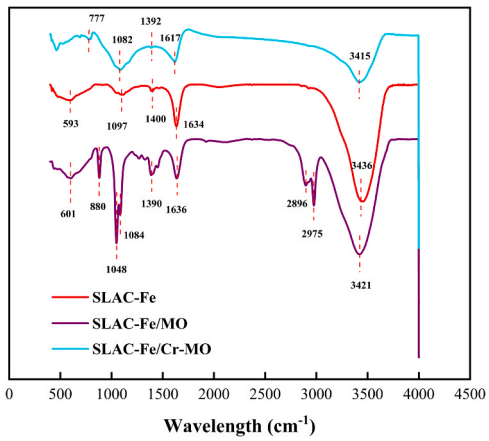

Fig. 4. FITR of SLAC-Fe in signal-component system and binary-component system.

and the peak intensity at 1082 cm^{-1} increased. The low peak appearing at 777 cm^{-1} was assigned to C–H bend in the aromatic groups (Ding et al., 2020). The band representing Si–O–Si disappeared. Compared with the infrared spectra of SLAC-Fe/MO, the intensity and number of the peaks in the SLAC-Fe/Cr-MO, were greatly reduced. It might be explained as follows: On the one hand, Cr^{6+} might be more easily adsorbed by biochar than MO; on the other hand, biochar might absorb more pollutants in the binary system than in the signal system.

3.1.4. XPS analyses

The chemical composition of SLAC-Fe before and after adsorption were investigated by XPS. As described in Fig. 5(a), the spectra of C1s, O1s and N1s were enhanced after adsorption, and a new peak (577.03 eV) corresponding to Cr2p appeared on the surface of SLAC-Fe/Cr-MO, which proved the successful adsorption of Cr^{6+} and MO. In order to provide more accurate information about the adsorption process, the high resolution XPS spectra of C1s, N1s and Cr2p are shown in Fig. 5(b), (c) and (d). In Fig. 5(b), the regions of 284.8 and 285.7 eV on the SLAC-Fe/Cr-MO represented C1s. The peak centered at 284.8 eV was attributed to the C atoms in the C–C and C=C bonds from surface amorphous C, while the weak peak at 285.7 eV might be due to the C atoms in C-OH (Mohammad et al., 2019). In Fig. 5(c), the N1s spectra of SLAC-Fe/Cr-MO at 398.7, 400.2 and 402.9 eV were attributed to the sp^2-hybridized aromatic N atoms bonding with C atoms (C=N–C), methyl group (N-CH_3) and silicon dioxide group, respectively (Mohammad et al., 2019). As shown in Fig. 5(d), the Cr2p region including components of Cr2p1/2 and Cr2p3/2 generated three pairs of spin-orbit doublet peaks. The XPS spectra of SLAC-Fe/Cr-MO located at 584.20 and 575.04 eV were related to Cr^{3+}, which were driven by Cr2p1/2 and Cr2p3/2, indicating the existence of Cr^{6+} in $Cr_2O_7^{2-}$ (Mao et al., 2012). The peaks located at 588.33 and 579.19 eV corresponded to Cr_2O_3. These results suggested that the Cr^{6+} was reduced to Cr^{3+} due to the existence of oxygen-containing functional groups on the surface of SLAC-Fe.

3.2. Adsorption performances of MO onto SLAC-Fe

3.2.1. Effect of initial pH

The effect of initial pH on the removal efficiencies of MO in aqueous solution was assessed, and the corresponding curves are shown in Fig. 6 (a). The pH-dependent experiment of SLAC and SLAC-Fe was carried out in the range of pH 2–10 when other parameters remained constant: contact time 30 min, temperature 25 °C, adsorbent dosage 4 g/L, initial MO concentration 40 mg/L. It can be seen that the SLAC and SLAC-Fe showed a trend of first increasing and then decreasing in the removal rate of MO, and the corresponding maximum values of 86.9% and 95.6% were observed at pH of 4.0, respectively. Therefore, pH = 4 was selected as the best adsorption condition.

This result can be explained by the change of H^+ density and surface charges of the adsorbent, which affected the electrostatic interaction between the adsorbent and the adsorbate (Alshameri et al., 2014). When the pH of aqueous solution was below the isoelectric point of the adsorbent, the surface of adsorbents was positively charged and could attract the anionic pollutants of MO. Simultaneously, iron on the SLAC-Fe existed in the form of ions under the acidic condition, which

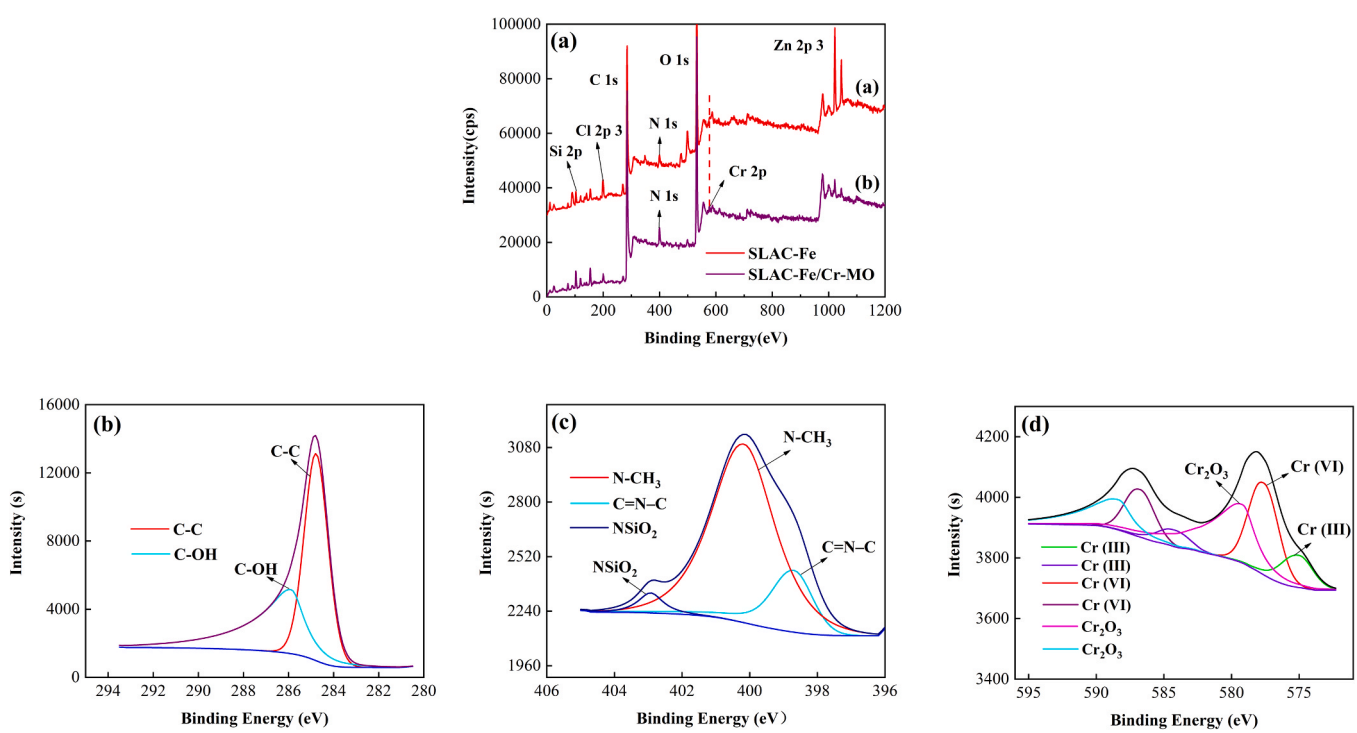

Fig. 5. (a) XPS wide scan of SLAC-Fe and SLAC-Fe/Cr-MO, (b) C 1s of SLAC-Fe/Cr-MO, (c) N 1s of SLAC-Fe/Cr-MO, (d) Cr 2p of SLAC-Fe/Cr-MO.

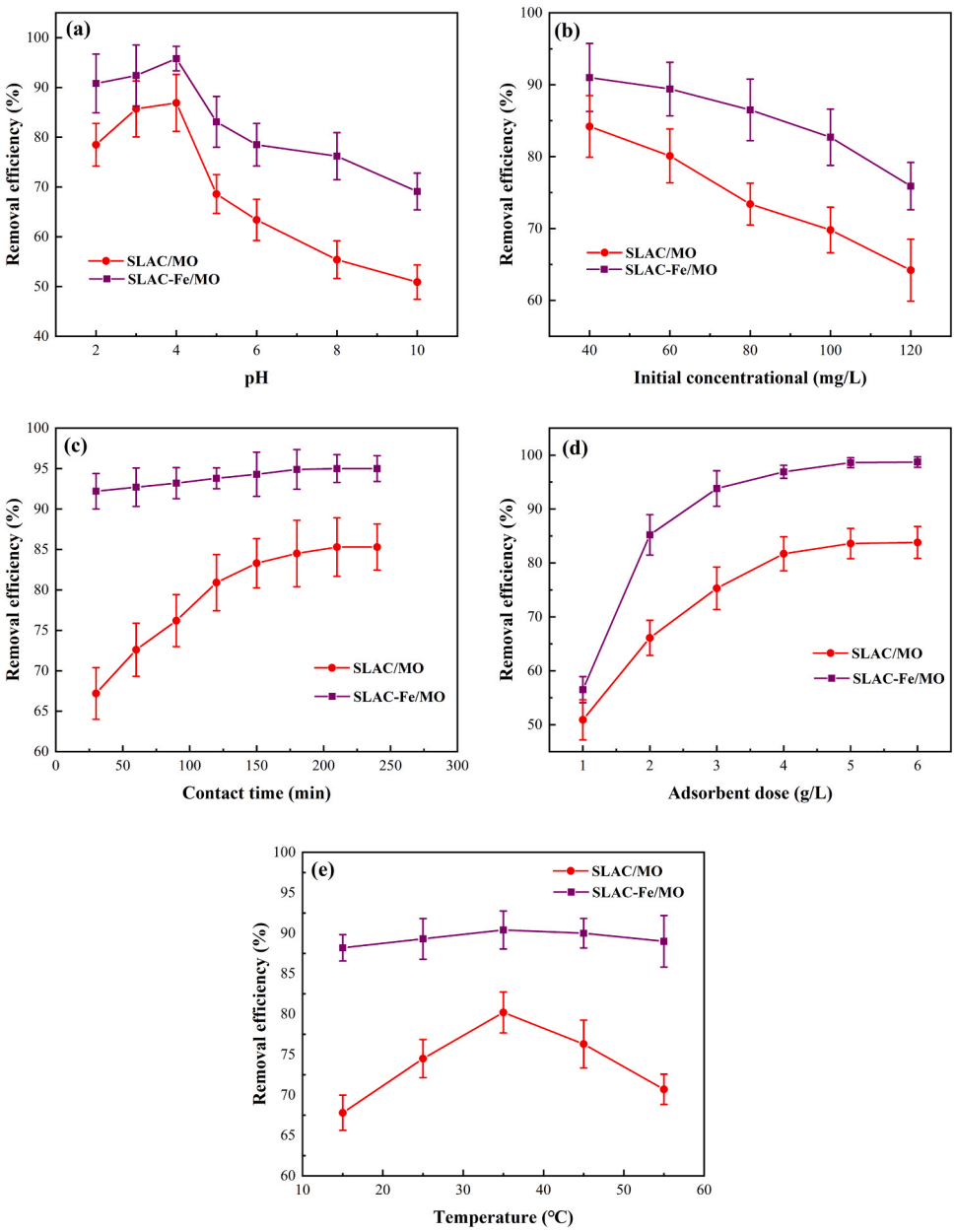

Fig. 6. Impact of operational parameters on adsorption of MO onto biochar.

also increased the electrostatic attraction of biochar to MO. As the pH value increased, especially when it exceeded 8, the iron mainly existed in the form of iron hydroxide, resulting in the decrease of the positive charges on the surface of adsorbent. Therefore, the electrostatic interaction between the biochar and MO was weakened, thereby reducing the removal efficiency of MO.

3.2.2. *Effect of initial concentration*

Adsorbate concentration is a significant parameter in adsorption studies, so the effect of initial MO concentration on the removal efficiency was studied. In this study, the initial MO concentration varied from 40 to 120 mg/L under the conditions of pH 4, contact time 30 min, temperature 25 °C, and adsorbent dose 4 g/L. It can be seen from Fig. 6 (b), with the increase of the initial MO concentration, the removal efficiencies of SLAC and SLAC-Fe to MO gradually decreased from 84.2% and 91% to 64.2% and 75.9%, respectively. It is generally believed that the driving force of the adsorption process increased with the increase of adsorbate concentration (Chakraborty et al., 2018). However, the results in this study were different. It might be explained by the fact that a certain amount of biochar provided a limited number of adsorption sites, and too high concentration of MO inevitably caused excessive crowding and adsorption barriers at the adsorption sites. Moreover, SLAC-Fe had a larger specific surface area than SLAC and provided more adsorption point sites for MO, leading to higher removal efficiency.

3.2.3. *Effect of contact time*

The effect of contact time (30–240 min) on the removal efficiencies of MO in aqueous solution was investigated under the conditions of an adsorbent dose of 4 g/L, a pH of 4, an initial MO concentration of 40 mg/L and a temperature of 25 °C. As shown in Fig. 6(c), the removal rate of MO remained above 90% with SLAC-Fe as adsorbent, while the removal rate of MO by SLAC increased rapidly from 67.2% to 84.5%, and then maintained stable. The result indicated that SLAC-Fe had a faster adsorption speed than SLAC. The rapid adsorption might be partly attributed to more available active sites and bigger driving force at the initial stage of adsorption (Devi and Saroha, 2017). As the adsorption

process progressed, the adsorption point tended to be saturation, resulting in an equilibrium between the adsorption and desorption process.

3.2.4. Effect of biochar dosage

The adsorbent dosage plays a crucial role in the adsorption process. When other parameters were set as follows: contact time 30 min, pH 4, initial MO concentration 40 mg/L and temperature of 25 °C, the effects of biochar dosage, in the range of 1–6 g/L, on the MO removal are shown in Fig. 6(d). As the biochar dosage increased from 1 to 4 g/L, the removal efficiencies of SLAC and SLAC-Fe on MO were improved to 82.1% and 93.3% from 48.2% and 36.4%, respectively. This is justified as the adsorption surface area and the availability of active sites increased with the increase of biochar dosage (Feng et al., 2015). With the further increase of biochar dosage, there was not obvious change. This is because when the adsorbent was increased to a certain extent, the overlap of active sites not only reduced the contact chance between biochar and MO, but also increased the length of the diffusion path (Garg et al., 2004). The higher removal rate of SLAC-Fe at dosage of 6 g/L might be due to its larger pore diameter, which reduced the overlapping possibility of active sites and did not hinder the adsorption path of MO.

3.2.5. Effect of temperature

In this study, the temperature ranged from 15 to 55 °C, with the contact time of 30 min, pH of 4, initial MO concentration of 40 mg/L and adsorbent dose of 4 g/L. In the Fig. 6(e), with the increase of temperature from 15 °C to 35 °C, the removal rate of SLAC to MO increased from 67.8% to 87.2%, and the corresponding value of SLAC-Fe increased from 88.2% to 90.4%. It indicated that the adsorption process was an endothermic reaction. Because the kinetic energy of MO molecules improved with the increase of temperature, which increased the probability of MO molecules contacting the active sites of biochar. However, the removal efficiency dropped down when the temperature continued to rise from 35 to 55 °C. The main reason for the decrease of removal rate might be that high temperature led to the kinetic energy of MO molecules exceeded the attraction potential of biochar to MO molecules (Mor et al., 2007).

3.3. Adsorption kinetics

To further examine the MO adsorption of SLAC and SLAC-Fe, the experimental data from the adsorption kinetics were analyzed by the pseudo-first-order and pseudo-second-order kinetic models. The applicability of these two kinetic models was tested by linear fitting (Fig. 7), and the corresponding parameters were listed in Table 2. The straight line was fitted well by the pseudo-second-order model and the correlation coefficient (R^2) was higher than 0.99, which presented a better match with the adsorption kinetics data than the line referred to the pseudo-first-order model. In addition, the calculated value of the equilibrium adsorption capacity (q_e^{cal}) (SLAC = 8.68 mg/g, SLAC-Fe = 9.57 mg/g) of the pseudo-second-order model was closer to the experimental value (q_e^{exp}) (SLAC = 8.54 mg/g, SLAC-Fe = 9.50 mg/g) than that of the pseudo-first-order model (q_e^{cal}) (SLAC = 0.90 mg/g, SLAC-Fe = 4.40 mg/g). Hence, the pseudo-second-order kinetic model was more suitable to interpret the adsorption kinetics of MO by the biochar.

Table 2
Parameters in the two kinetic models for MO adsorption by biochar.

Kinetic models Related parameters	q_e^{exp} (mg/g)	Pseudo-first-order			Pseudo-second-order		
		k_1 (1/min)	q_e^{cal} (mg/g)	R^2	K_2 (g/(mg/min))	q_e^{cal} (mg/g)	R^2
SLAC	8.54	0.014	0.90	0.987	0.031	8.68	0.999
SLAC-Fe	9.50	0.011	4.40	0.958	0.055	9.57	0.999

3.4. Effect of Cr^{6+} on MO adsorption

The multi-component adsorption system is more representative of the composition of actual wastewater. The study of biosorption equilibrium is very important in multi-component system, because it is not only affected by the surface properties and operating conditions, but also by the competition between different pollutants for active sites (Ding et al., 2020). In this work, the adsorption of MO by biochar in the presence of Cr^{6+} was investigated. At the same time, SLAC-Fe was selected as the adsorbent, and the experimental conditions were determined through the single factor control experiment. The parameters were set as: adsorbent dose 4 g/L, pH 4, contact time 30 min and temperature of 25 °C. It can be seen from Fig. 8(a), that the presence of Cr^{6+} affected the removal efficiency of MO. When the concentrations of Cr^{6+} were 0 mmol/L, 0.2 mmol/L and 0.8 mmol/L, the highest removal efficiencies of MO were 96.5%, 95.8% and 94.2%, respectively.

The relationship between the adsorption amount of adsorbate at adsorption equilibrium point and the concentration of adsorbate in aqueous phase was shown by adsorption isotherm. The experimental data of MO adsorption with the presence of Cr^{6+} were fitted to the Langmuir and Freundlich isotherms using the nonlinearization procedures, and to the Temkin isotherm using linearization procedure (in Fig. 8 (b), (c) and (d)). The estimated parameters are presented in Table 3. As displayed in Table 3, the experimental data of MO adsorption in the presence of Cr^{6+} were more consistent with Freundlich isotherm adsorption model. The R^2 values of Freundlich model (R^2 = 0.949, 0.861, 0.864) were larger than that of Langmuir model (R^2 = 0.913, 0.844, 0.845) and Temkin model (R^2 = 0.903, 0.842, 0.813), indicating

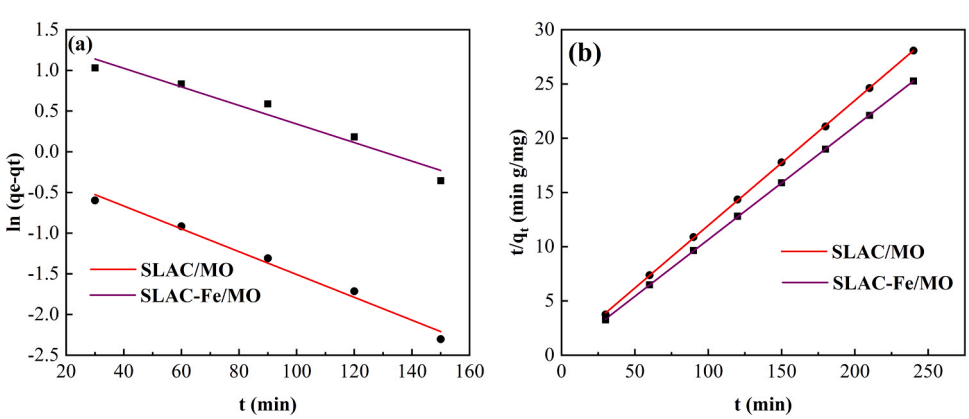

Fig. 7. (a) pseudo-first-order and (b) pseudo-second-order adsorption kinetics for MO adsorption onto biochar.

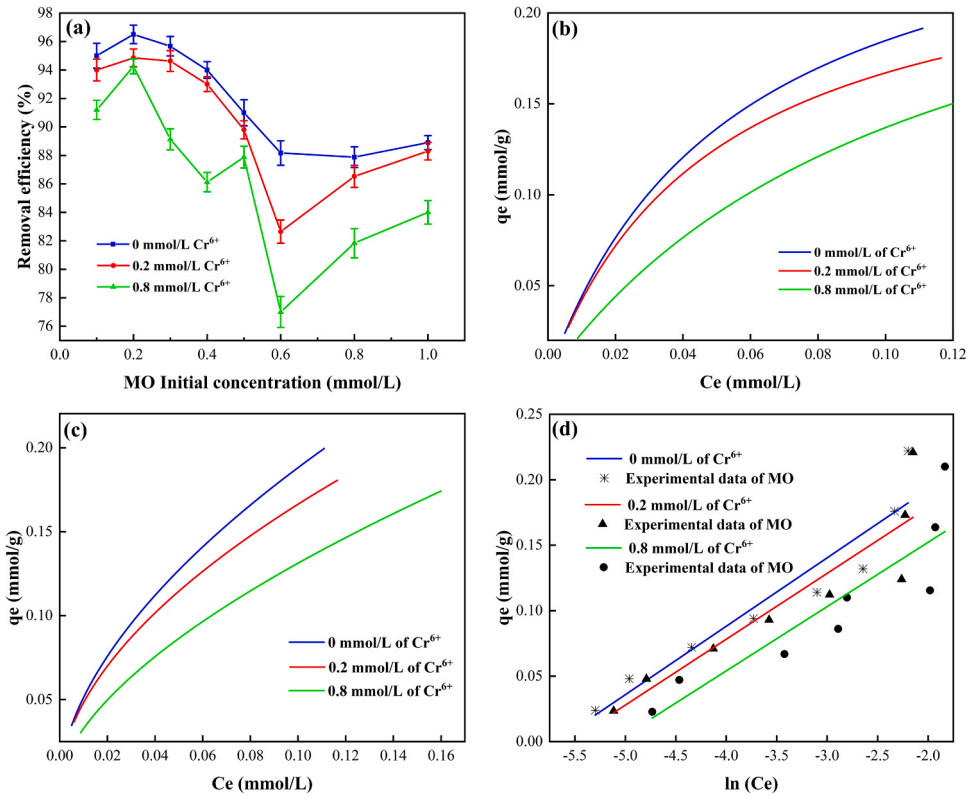

Fig. 8. (a) impact of MO concentration and Cr^{6+} concentration on adsorption of MO onto SLAC-Fe, (b) Langmuir, (c) Freundlich, (d) Temkin isotherms for MO with different concentrations of Cr^{6+} in equilibrium.

Table 3
Parameters of the Langmuir, Freundlich, Temkin isotherm models for MO with different concentrations of Cr^{6+} adsorption onto SLAC-Fe.

Cation	Langmuir model		
	Q_0 (mmol/g)	K_L (L/mmol)	R^2
MO-0 mmol/L of Cr^{6+}	0.29	18.18	0.913
MO-0.2 mmol/L of Cr^{6+}	0.26	15.89	0.844
MO-0.8 mmol/L of Cr^{6+}	0.22	10.62	0.845
	Freundlich model		
	K_F	n	R^2
MO-0 mmol/L of Cr^{6+}	0.69	1.72	0.949
MO-0.2 mmol/L of Cr^{6+}	0.57	1.86	0.861
MO-0.8 mmol/L of Cr^{6+}	0.53	1.66	0.864
	Temkin model		
	K_T	B	R^2
MO-0 mmol/L of Cr^{6+}	379.93	0.052	0.903
MO-0.2 mmol/L of Cr^{6+}	285.42	0.050	0.842
MO-0.8 mmol/L of Cr^{6+}	165.74	0.049	0.813

that the adsorption process was chemical and multilayer adsorption between SLAC-Fe and MO in single and binary systems.

The maximum adsorption uptake (Q_0) and equilibrium adsorption constant (K_L) were obtained from Langmuir isotherm model. As shown in Table 3, under different initial Cr^{6+} concentrations, the adsorption capacities of SLAC-Fe to MO in the binary system were lower than that of the single system. The Q_0 of SLAC-Fe to MO without Cr^{6+} was 0.29 mmol/g, while the Q_0 values of MO were 0.26 and 0.22 mmol/g with Cr^{6+} concentrations of 0.2 and 0.8 mmol/L, which decreased by 10.3% and 24.1%, respectively. Therefore, the presence of Cr^{6+} had a negative effect on the adsorption of MO. Furthermore, the K_L values for MO were 18.18, 15.89 and 10.62 L/mmol, respectively, indicating that the affinity of the SLAC-Fe to MO decreased with the increase of Cr^{6+}concentration.

Another parameter, separation factor (R_L), was used to confirm whether the adsorption process is good. R_L is given by the Eq. (8):

$$R_L = \frac{1}{1 + K_L C_0} \tag{8}$$

The value of R_L reflects the trend of adsorption: irreversible ($R_L = 0$), favorable ($0 < R_L < 1$), linear ($R_L = 1$), and unfavorable ($R_L > 1$)(Martins et al., 2015). In this experiment, the values of R_L in single and binary systems were less than 1, indicating that the adsorption process was favorable.

3.5. Adsorption mechanism

In the single system, MO in aqueous solution existed in the form of anion, and the adsorption of MO was achieved by electrostatic attraction which mainly through the attraction between SO_3^- and positively charged functional groups. In fact, hydrogen bonds might be formed between the molecular structures of MO and SLAC-Fe, such as the nitrogen atoms in MO form hydrogen bonds with -OH or $-NH_2$ (Mohammad et al., 2019).

In the binary system of MO and Cr^{6+}, the coexistence of Cr^{6+} significantly affected the adsorption of MO, and SLAC-Fe had a preference for Cr^{6+} compared with MO. The K_L value in isothermal adsorption model of MO decreased with the increase of Cr^{6+} concentration, indicating that the affinity of SLAC-Fe to MO decreased. Meanwhile, the FTIR spectra of SLAC-Fe/MO and SLCA-Fe/Cr-MO also suggested that the functional groups on the surface of the biochar were involved in the chemical adsorption.

Therefore, the inhibition mechanism of Cr^{6+} on MO might be assigned into following aspects: $HCrO_4^-$ and $Cr_2O_7^{2-}$ competed with SO_3^- for effective adsorption sites on the surface of SLAC-Fe, simultaneously, some special adsorption sites favorable for $HCrO_4^-$ and $Cr_2O_7^{2-}$ were produced on the surface of the SLAC-Fe/MO. Another interaction was the electrostatic attraction between $HCrO_4^-$ and $Cr_2O_7^{2-}$ and positively

charged functional groups (Fe^{3+} and N–CH_3^+ of MO) on the surface of SLAC-Fe or SLAC-Fe/MO, which increased the adsorption potential of Cr^{6+}. Then, the adsorbed Cr^{6+} was partly reduced to Cr^{3+} through oxygen-containing functional groups, such as Si–O–Si, -OH and Fe^{3+}. Other interaction was that the ion exchange between $HCrO_4^-/Cr_2O_7^{2-}$ and Cl^- on the surface of SLAC-Fe was stronger than that of MO, making it easier for Cr^{6+} to enter the biochar through the pores. After adsorption, chromium oxide was formed in the process of separation and drying activated carbon (Eqs. (9)–(13)).

$$Cr_2O_7^{2-} + H_2O \leftrightarrow 2\ HCrO_4^- \tag{9}$$

$$3A - OH + HCrO_4^- + 4H^+ \leftrightarrow 3A - O + Cr^{3+} + 4H_2O \tag{10}$$

$$3Si - O - Si + 3HCrO_4^- + 5H^+ \leftrightarrow 3Si - O + 3SiCr^{3+} + 4H_2O \tag{11}$$

$$Cr^{3+} + 3OH^- \leftrightarrow Cr(OH)_3 \tag{12}$$

$$2Cr(OH)_3 \leftrightarrow Cr_2O_3 + 3H_2O \tag{13}$$

4. Conclusions

This study showed that SLAC-Fe was a more effective adsorbent for the removal of MO than SLAC due to its better pore structure and functional groups. The optimal operational parameters of SLAC-Fe for MO adsorption were determined, in single system, and the kinetic model of pseudo-second-order fitted well to the experimental data. Furthermore, in the binary system with Cr^{6+} existence, the maximum adsorption capacity for MO decreased proportionally with the increase of Cr^{6+} concentration. Simultaneously, the equilibrium experimental data of MO were in good agreement with the Freundlich isotherm model. The adsorption process of SLAC-Fe on MO was based on chemical and multilayer adsorption. The active sites on SLAC-Fe, such as -OH, N–H, $-NH_2$ Si–O–Si, had a higher affinity for $HCrO_4^-$ and $Cr_2O_7^{2-}$ than SO_3^-, resulting in a reduction in the adsorption capacity of MO in the presence of Cr^{6+}.

CRediT authorship contribution statement

Yali Liu: Conceptualization, Methodology, Software **Han Cheng**: Data curation, Writing- Original draft preparation. **Xin Li**: Visualization, Investigation. **Han Cheng**: Supervision.: **Han Cheng**: Software, Validation.: **Yali Liu:** Writing- Reviewing and Editing. All authors have read and agreed to the published version of the manuscript.

Declaration of Competing Interest

The authors declare that they have no known competing financial interests or personal relationships that could have appeared to influence the work reported in this paper.

Acknowledgement

This work was financially supported by the Nanjing Forestry University Youth Innovation Fund, China, (Grant number. CX2017025), and the National Natural Science Foundation of China, China, (Grant No. 51608272).

References

Agrafioti, E., Kalderis, D., Diamadopoulos, E., 2014. Ca and Fe modified biochars as adsorbents of arsenic and chromium in aqueous solutions. J. Environ. Manage. 146, 444–450.
Aksu, Z., Acikel, U., Kabasakal, E., Tezer, S., 2002. Equilibrium modelling of individual and simultaneous biosorption of chromium(VI) and nickel(II) onto dried activated sludge. Water Res. 36, 3063–3073.
Alam, M.M., Hossain, M.A., Hossain, M.D., Johir, M.A.H., Hossen, J., Rahman, M.S., Zhou, J.L., Hasan, A.T.M.K., Karmakar, A.K., Ahmed, M.B., 2020. The potentiality of rice husk-derived activated carbon: from synthesis to application. Processes 8, 203.
Alshameri, A., Ibrahim, A., Assabri, A.M., Lei, X., Wang, H., Yan, C., 2014. The investigation into the ammonium removal performance of Yemeni natural zeolite: modification, ion exchange mechanism, and thermodynamics. Powder Technol. 258, 20–31.
Chakraborty, P., Show, S., Banerjee, S., Halder, G., 2018. Mechanistic insight into sorptive elimination of ibuprofen employing bi-directional activated biochar from sugarcane bagasse: performance evaluation and cost estimation. J. Environ. Chem. Eng. 6, 5287–5300.
Chen, G., Wang, X., Li, J., Yan, B., Wang, Y., Wu, X., Velichkova, R., Cheng, Z., Ma, W., 2019. Environmental, energy, and economic analysis of integrated treatment of municipal solid waste and sewage sludge: a case study in China. Sci. Total Environ. 647, 1433–1443.
Devi, P., Saroha, A.K., 2017. Utilization of sludge based adsorbents for the removal of various pollutants: a review. Sci. Total Environ. 578, 16–33.
Ding, J., Pan, Y., Li, L., Liu, H., Zhang, Q., Gao, G., Pan, B., 2020. Synergetic adsorption and electrochemical classified recycling of Cr(VI) and dyes in synthetic dyeing wastewater. Chem. Eng. J. 384, 123232.
Enniya, I., Rghioui, L., Jourani, A., 2018. Adsorption of hexavalent chromium in aqueous solution on activated carbon prepared from apple peels. Sustain. Chem. Pharm. 7, 9–16.
Feng, J., Qiao, K., Pei, L., Lv, J., Xie, S., 2015. Using activated carbon prepared from Typha orientails Presl to remove phenol from aqueous solutions. Ecol. Eng. 84, 209–217.
Ferrero, F., 2007. Dye removal by low cost adsorbents: hazelnut shells in comparison with wood sawdust. J. Hazard. Mater. 142, 144–152.
Fierro, V., Muniz, G., Gonzalez-Sanchez, G., Ballinas, M.L., Celzard, A., 2009. Arsenic removal by iron-doped activated carbons prepared by ferric chloride forced hydrolysis. J. Hazard. Mater. 168, 430–437.
Gan, C., Liu, Y., Tan, X., Wang, S., Zeng, G., Zheng, B., Li, T., Jiang, Z., Liu, W., 2015. Effect of porous zinc-biochar nanocomposites on Cr(VI) adsorption from aqueous solution. RSC Adv. 5, 35107–35115.
Garg, V.K., Kumar, R., Gupta, R., 2004. Removal of malachite green dye from aqueous solution by adsorption using agro-industry waste: a case study of Prosopis cineraria. Dyes Pigments 62, 1–10.
Gholami, P., Khataee, A., Soltani, R.D.C., Dinpazhoh, L., Bhatnagar, A., 2020. Photocatalytic degradation of gemifloxacin antibiotic using Zn–Co-LDH@biochar nanocomposite. J. Hazard. Mater. 382, 121070.
Ghorbani, F., Kamari, S., Zamani, S., Akbari, S., Salehi, M., 2020. Optimization and modeling of aqueous Cr(VI) adsorption onto activated carbon prepared from sugar beet bagasse agricultural waste by application of response surface methodology. Surfa. Interf. 18, 100444.
Hu, Y., Quan, C., Guo, M., Ye, X., Wu, Z., 2017. Preparation of Fe_3O_4-octadecyltrichlorosilane for removal of methyl orange and methylene blue: influence of ph and ionic strength on competitive adsorption. J. Wuhan Univ. Technol. Mater. Sci. Ed. 32, 1413–1419.
Jawad, A.H., Mamat, N.F.H., Hameed, B.H., Ismail, K., 2019. Biofilm of cross-linked Chitosan-Ethylene Glycol Diglycidyl Ether for removal of Reactive Red 120 and Methyl Orange: adsorption and mechanism studies. J. Environ. Chem. Eng. 7, 102965.
Kafshgari, L.A., Ghorbani, M., Azizi, A., 2017. Fabrication and investigation of $MnFe_2O_4$/MWCNTs nanocomposite by hydrothermal technique and adsorption of cationic and anionic dyes. Appl. Surf. Sci. 419, 70–83.
Lian, F., Sun, B., Song, Z., Zhu, L., Qi, X., Xing, B., 2014. Physicochemical properties of herb-residue biochar and its sorption to ionizable antibiotic sulfamethoxazole. Chem. Eng. J. 248, 128–134.
Liu, W., Zhang, J., Zhang, C., Wang, Y., Li, Y., 2010. Adsorptive removal of Cr (VI) by Fe-modified activated carbon prepared from Trapa natans husk. Chem. Eng. J. 162, 677–684.
Luna, A.S., Costa, A.L.H., da Costa, A.C.A., Henriques, C.A., 2010. Competitive biosorption of cadmium(II) and zinc(II) ions from binary systems by Sargassum filipendula. Bioresour. Technol. 101, 5104–5111.
Ma, H., Yang, J., Gao, X., Liu, Z., Liu, X., Xu, Z., 2019. Removal of chromium (VI) from water by porous carbon derived from corn straw: influencing factors, regeneration and mechanism. J. Hazard. Mater. 369, 550–560.
Mahmoud, M.E., Amira, M.F., Seleim, S.M., Mohamed, A.K., 2020. Amino-decorated magnetic metal-organic framework as a potential novel platform for selective removal of chromium (Vl), cadmium (II) and lead (II). J. Hazard. Mater. 381, 120979.
Mao, N., Yang, L., Zhao, G., Li, X., Li, Y., 2012. Adsorption performance and mechanism of Cr(VI) using magnetic PS-EDTA resin from micro-polluted waters. Chem. Eng. J. 200, 480–490.
Martins, A.C., Pezoti, O., Cazetta, A.L., Bedin, K.C., Yamazaki, D.A.S., Bandoch, G.F.G., Asefa, T., Visentainer, J.V., Almeida, V.C., 2015. Removal of tetracycline by NaOH-activated carbon produced from macadamia nut shells: kinetic and equilibrium studies. Chem. Eng. J. 260, 291–299.
Mohammad, A.T., Abdulhameed, A.S., Jawad, A.H., 2019. Box-Behnken design to optimize the synthesis of new crosslinked chitosan-glyoxal/TiO_2 nanocomposite: methyl orange adsorption and mechanism studies. Int. J. Biol. Macromol. 129, 98–109.
Mor, S., Ravindra, K., Bishnoi, N.R., 2007. Adsorption of chromium from aqueous solution by activated alumina and activated charcoal. Bioresour. Technol. 98, 954–957.

Nur, T., Loganathan, P., Nguyen, T.C., Vigneswaran, S., Singh, G., Kandasamy, J., 2014. Batch and column adsorption and desorption of fluoride using hydrous ferric oxide: Solution chemistry and modeling. Chem. Eng. J. 247, 93–102.
Qian, W., Zhao, A.Z., Xu, R.K., 2013. Sorption of As(V) by aluminum-modified crop straw-derived biochars. Water Air Soil Pollut. 224, 1610.
Qiu, M., Wang, M., Zhao, Q., Hu, B., Zhu, Y., 2018. XANES and EXAFS investigation of uranium incorporation on nZVI in the presence of phosphate. Chemosphere 201, 764–771.
Qiu, M., Liu, Z., Wang, S., Hu, B., 2020. The photocatalytic reduction of U(VI) into U(IV) by ZIF-8/g-C3N4 composites at visible light. Environ. Res., 110349 https://doi.org/10.1016/j.envres.2020.110349.
Ruiz-Gomez, N., Quispe, V., Abrego, J., Atienza-Martinez, M., Benita Murillo, M., Gea, G., 2017. Co-pyrolysis of sewage sludge and manure. Waste Manag. 59, 211–221.
Setshedi, K.Z., Bhaumik, M., Songwane, S., Onyango, M.S., Maity, A., 2013. Exfoliated polypyrrole-organically modified montmorillonite clay nanocomposite as a potential adsorbent for Cr(VI) removal. Chem. Eng. J. 222, 186–197.
Silva, T.L., Cazetta, A.L., Souza, P.S.C., Zhang, T., Asefa, T., Almeida, V.C., 2018. Mesoporous activated carbon fibers synthesized from denim fabric waste: efficient adsorbents for removal of textile dye from aqueous solutions. J. Clean. Prod. 171, 482–490.
Sugashini, S., Begum, K., 2014. Performance of Fe-loaded chitosan carbonized rice Husk Beads (Fe-CCRB) for continuous adsorption of metal ions from industrial effluents. Environ. Prog. Sustain. 33, 1125–1138.
Thuy Chung, N., Loganathan, P., Tien Vinh, N., Vigneswaran, S., Kandasamy, J., Naidu, R., 2015. Simultaneous adsorption of Cd, Cr, Cu, Pb, and Zn by an iron-coated Australian zeolite in batch and fixed-bed column studies. Chem. Eng. J. 270, 393–404.
Tian, Y., Yang, F., 2007. Reduction of hexavalent chromium by polypyrrole-modified steel mesh electrode. J. Clean. Prod. 15, 1415–1418.
Tuna, A.O.A., Ozdemir, E., Simsek, E.B., Beker, U., 2013. Optimization of process parameters for removal of arsenic using activated carbon-based iron-containing adsorbents by response surface methodology. Water Air Soil Pollut. 224, 1685.
Valentin-Reyes, J., Garcia-Reyes, R.B., Garcia-Gonzalez, A., Soto-Regalado, E., Cerino-Cordova, F., 2019. Adsorption mechanisms of hexavalent chromium from aqueous solutions on modified activated carbons. J. Environ. Manag. 236, 815–822.
Wang, H., Yang, N., Qiu, M., 2020. Adsorption of Cr(VI) from aqueous solution by biochar-clay derived from clay and peanut shell. J. Inorg. Mater. 35, 301–308.
Yu, Z., Song, W., Li, J., Li, Q., 2020. Improved simultaneous adsorption of Cu(II) and Cr (VI) of organic modified metakaolin-based geopolymer. Arab. J. Chem. 13, 4811–4823.
Zhang, B., Wu, Y., Cha, L., 2020. Removal of methyl orange dye using activated biochar derived from pomelo peel wastes: performance, isotherm, and kinetic studies. J. Disper. Sci. Technol. 41, 125–136.
Zhang, Z.H., Zhang, J.L., Liu, J.M., Xiong, Z.H., Chen, X., 2016. Selective and competitive adsorption of azo dyes on the metal-organic framework ZIF-67. Water Air Soil Pollut. 227, 471.
Zhao, Q.L., Wang, X.Y., Xia, H., Liu, J., Wang, H., Gao, J., Zhang, Y.W., Liu, J., Zhou, H. Y., Li, X.L., Zhang, S.Y., Wang, X.Y., 2015. Design, preparation and performance of novel three-dimensional hierarchically porous carbon for supercapacitors. Electrochim. Acta 173, 566–574.
Zhong, D., Zhang, Y., Wang, L., Chen, J., Jiang, Y., Tsang, D.C.W., Zhao, Z., Ren, S., Liu, Z., Crittenden, J.C., 2018. Mechanistic insights into adsorption and reduction of hexavalent chromium from water using magnetic biochar composite: Key roles of Fe_3O_4 and persistent free radicals. Environ. Pollut. 243, 1302–1309.
Zhong, X., Lu, Z., Liang, W., Hu, B., 2020. The magnetic covalent organic framework as a platform for high-performance extraction of Cr(VI) and bisphenol a from aqueous solution. J. Hazard. Mater. 393, 122353.
Zhong, X., Liang, W., Lu, Z., Hu, B., 2020. Highly efficient enrichment mechanism of U (VI) and Eu(III) by covalent organic frameworks with intramolecular hydrogen-bonding from solutions. Appl. Surf. Sci. 504, 144403.
Zhou, X., Liu, Y., Zhou, J., Guo, J., Ren, J., Zhou, F., 2018. Efficient removal of lead from aqueous solution by urea-functionalized magnetic biochar: preparation, characterization and mechanism study. J. Taiwan Inst. Chem. E. 91, 457–467.
Zou, W., Liu, L., Li, H., Han, X., 2016. Investigation of synergistic adsorption between methyl orange and Cd(II) from binary mixtures on magnesium hydroxide modified clinoptilolite. Korean J. Chem. Eng. 33, 2073–2083.